ADVANCED FUNCTIONAL MATERIALS
www.afm-journal.de

NIR-Triggered $Cu_2O/Cu_{2-x}S$ Heterostructure as an "All-In-One" Functional Nanoplatform for Efficient Synergistic Tumor Therapy

Weihua Gao, Jie Zhang, Yi Chang, Fangli Gao, Guanglei Ma, Zhiyong Gao, Xiaobing Wang, Xinhe Liu, Xiaoming Ma,* and Yuming Guo**

The fabrication of synergistic multifunctional anti-tumor nanoplatforms is challenging due to the urgent requirement to activate different therapeutic modalities. Although the multi-modal treatments can be achieved by carrying out the activation with different exogenous and endogenous stimulations in sequence, this tedious manner is not applicable to the ideal synergistic cancer treatment. Herein, a simple heterojunction of $Cu_2O/Cu_{2-x}S$ modified with gambogic acid and hyaluronic acid (CCS@GA@HA) is ingeniously fabricated for the synergistic cancer treatment combining photothermal therapy (PTT), photocatalytic therapy (PCT), chemodynamic therapy (CDT) and potential ferroptosis just activated by the single near infrared (NIR) light irradiation. $Cu_2O/Cu_{2-x}S$ heterostructure (CCS) with promoted separation and transfer efficiency of photogenerated charge carriers exhibits excellent photocatalytic performance. The intervention of gambogic acid (GA) downregulates the overexpression of heat shock protein 90 (HSP90), which make it possible to execute the mild PTT. And the CDT performance is efficiently improved by the heat generated from PTT. Specifically, CCS appears to accelerate the accumulation of lipid peroxides (LPO) and inactivate glutathione peroxidase 4 (GPX4) that directly induce ferroptosis. In brief, CCS@GA@HA exhibits prominent NIR-triggered synergistic effect involving PCT, mild PTT, enhanced CDT and ferroptosis for an effective multi-modal tumor treatment.

1. Introduction

The treatment of cancer is directly related to the quality of human life and health, which has been the hot exploring field to researchers and clinicians[1,2] Although the treatment of cancer has made great progress in recent years, the severe adverse effects, multidrug resistance and metastasis have made the therapeutic performance of traditional cancer treatments, such as chemotherapy, radiotherapy and surgery, far from satisfactory.[3–5] To overcome the dilemma of traditional cancer therapy and reduce postoperative adverse events, various kinds of therapeutic modalities, such as photothermal therapy (PTT),[6,7] chemodynamic therapy (CDT),[8–10] photodynamic therapy (PDT),[11,12] sonodynamic therapy (SDT),[13] ultrasound therapy (UST), immunotherapy,[14,15] and ferroptosis,[16] have been extensively explored. However, due to the complexity of different cancers, the stand-alone treatment strategy usually just shows poor therapeutic efficiency and there may not be a satisfactory single treatment prescription for cancer treatment.

The combination therapy that integrate one strategy with other treatment options appears to own good therapeutic efficiency in cancer treatment.[17–19] As we know, surgery combined with immunotherapy have already exhibited good clinical application prospects.[20,21] Promoted by the significant advancement of nanotechnology, nanomedicines with intrinsic functional characteristics, stronger design flexibility, and specific responsiveness to tumor microenvironment (TME), are easier to achieve the combination therapy by involving a certain number of therapeutic modalities derived from different components.[22–24] For example, the drug-loaded delivery system can be simply converted to a combined cancer treatment system by just adopting a nanocarrier with certain kind of cancer therapeutic modality.[25–27] The physical fusion of nanomaterials (NMs) with different cancer therapeutic modality is another main way to achieve the combination therapy.[28] Such examples could be multiplied indefinitely in recent years.[29,30] However, the design and synthesis of nanomedicines for the combination cancer therapy are still the highly innovative and challenging topic. Currently, it is worth noting that the core idea in constructing a combination therapy system is no longer the simple superimposition of the

W. Gao, J. Zhang, Y. Chang, F. Gao, Z. Gao, X. Liu, Y. Guo
School of Chemistry and Chemical Engineering
Henan Normal University
Xinxiang, Henan 453007, China
E-mail: yc0906@htu.edu.cn; guoyuming@htu.edu.cn
G. Ma, X. Wang, X. Ma
Key Laboratory of Green Chemical Media and Reactions
Ministry of Education
Henan Normal University
Xinxiang, Henan 453007, China
E-mail: mxm@htu.edu.cn

The ORCID identification number(s) for the author(s) of this article can be found under https://doi.org/10.1002/adfm.202408125

DOI: 10.1002/adfm.202408125

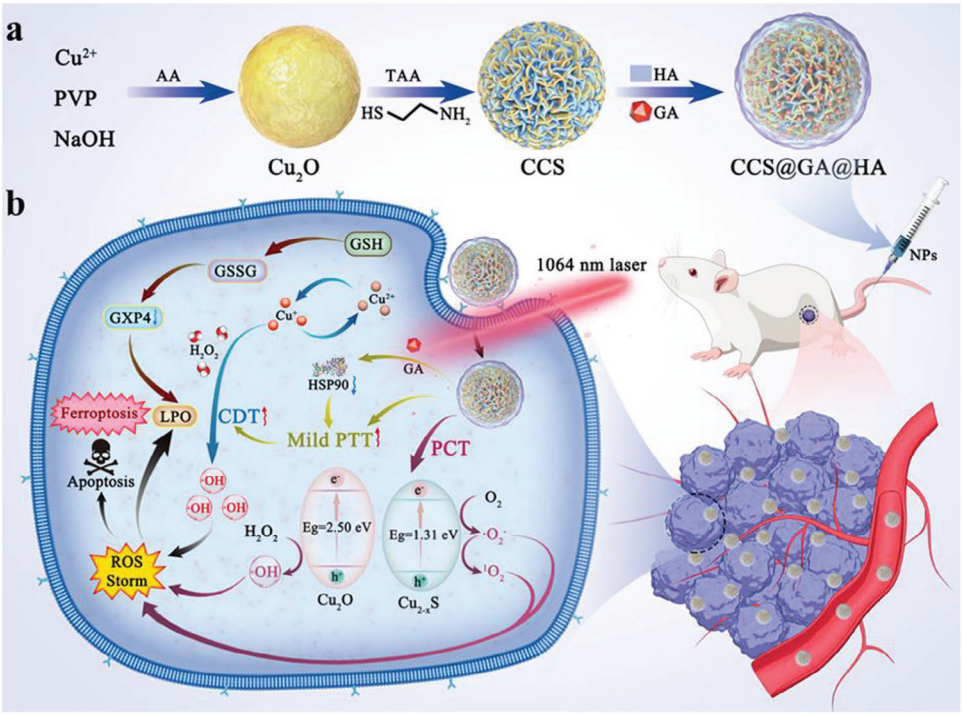

Scheme 1. Schematic illustration of a) the synthetic process of CCS@GA@HA and b) multi-modal treatments of CCS@GA@HA nanoplatforms.

different cancer therapeutic modalities. Instead, the focus of the research in this field has turned to the synergistic effect between different components to achieve a more desirable therapeutic effect compared with the corresponding individual cancer treatment.[31]

Recently, heterostructured semiconductor NMs used for photocatalytic therapy (PCT) of cancer have attracted increasing attention.[32–34] The heterojunction formed by coupling two different functional materials promotes the electron–hole separation, which overcomes the drawbacks of single component nanomedicine and can greatly improve the therapeutic performance.[35,36] Significantly, heterostructured semiconductor NMs containing different components have the novel derived unique functions while retaining the intrinsic property of single component.[37] Apart from other advantages, the rational design and fabrication of heterojunctions using different components are undoubtedly the more feasible and effective strategy to achieve the synergistic cancer therapy. In past years, heterostructured semiconductor NMs have been widely fabricated to provide unique and enhanced therapeutic modalities by virtue of their unique and excellent properties,[38] while just finite researches are related to the multi-modal synergistic cancer treatments.[39–43]

Herein, we designed a binary copper-based $Cu_2O/Cu_{2-x}S$@gambogic acid@hyaluronic acid (CCS@GA@HA) heterostructure as a coactivatable nanomedicine by TME and simple exogenous stimuli for the multi-modal synergistic treatment of cancer (**Scheme 1**). The CDT modality of CCS nanocomposites can be activated by the acidic TME. Overexpressed glutathione (GSH) was consumed and endogenous H_2O_2 was disintegrated to ·OH by the released redox couple (Cu^{2+}/Cu^{+}).[44] Meanwhile, the depletion of GSH not only induces tumor cell apoptosis by destroying the redox balance of tumor cells, but also promotes ferroptosis according to the inactivation of GPX4 and the accumulation of LPO.[45,46] The photothermal performance of CCS was triggered by the exogenous 1064 nm NIR-II laser irradiation, and it displayed a relatively high photothermal conversion property. Through the introduction of GA, the expression of HSP90 in cancer cells was down-regulated and low-temperature (≈43 °C) PTT with efficient tumor destruction was achieved simultaneously. Meanwhile, the temperature increasing at tumor site, in turn, helped to augment the CDT performance by accelerating the Fenton-like reaction rate to increase the ·OH yield.[47–49] Accompanied by the fabrication of heterostructure, CCS exhibited enhanced photo-induced carriers separation as well as the transfer efficiency under 1064 nm NIR-II laser irradiation, and thus derived the significant PCT modality. Under this modality, robust reactive oxygen species (ROS) were generated and intracellular oxidative stress triggered by PCT could further improved the cancer cell apoptosis and ferroptosis.[50,51] The modification of HA could improve the accumulation and uptake of CCS by CD44-overexpressed tumor cells to pursuit a more satisfactory therapeutic efficacy.[52] Consequently, we have successfully exploited a double stimulation coactivatable nanomedicine based on a simple heterostructure that ingeniously integrated PTT, PCT, CDT and ferroptosis for the treatment of cancer with high efficiency. It may provide a meaningful inspiration for the multi-modal synergistic treatment of cancer.

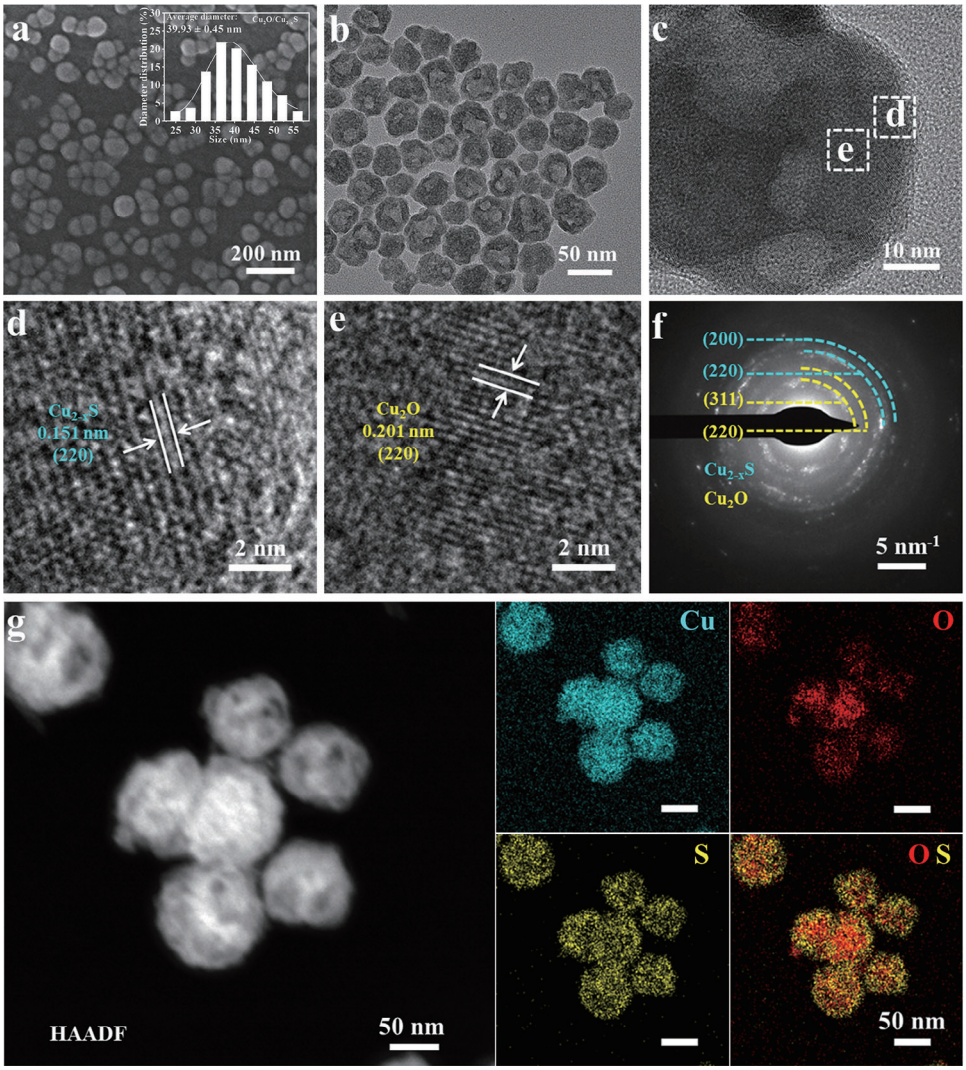

Figure 1. a) FE-SEM image and size distribution of CCS NPs (insert picture). b) TEM and c) HRTEM images of CCS NPs. d,e) were the corresponding images amplified from (c) HRTEM of CCS NPs. f) SEAD pattern of CCS NPs. g) The HAADF-STEM image and elemental mapping of Cu, O, and S.

2. Results and Discussion

2.1. Synthesis and Characterization of CCS@GA@HA

Herein, the CCS heterostructure was fabricated by an improved anion exchange strategy (Scheme 1a).[53] First, monodispersed Cu_2O nanospheres ≈35.59 nm were achieved as the template for subsequent synthesis of heterostructure (Figures S1 and S2, Supporting Information).[54] Then, the CCS heterostructure was simply fabricated by a mild reaction of Cu_2O precursor with the thioacetamide (TAA) and 2-aminoethanethiol solution. From the field emission scanning electron microscopy (FE-SEM) and transmission electron microscopy (TEM) images (**Figure** 1a,b), it can be clearly seen that the synthesized CCS have displayed as highly dispersed nanoparticles (NPs) with an average diameter of 39.93 nm, slightly bigger than that of Cu_2O precursors. Furthermore, the formation of heterojunction can be verified by the high resolution TEM (HR-TEM) images (Figure 1c-e), the lattice fringes of $Cu_{2-x}S$ (d220 = 0.151 nm) and Cu_2O (d220 = 0.201 nm) are well distributed in CCS NPs, and the emergence of $Cu_{2-x}S$ also can be verified by the diffraction rings of $Cu_{2-x}S$ (blue) in the corresponding SAED images (Figure 1f).[55] To further figure out the composition of CCS heterostructures, elemental mapping images and high-angle annular dark field-scanning TEM (HAADF-STEM) were collected to prove the existence and distribution of different elements in the heterostructures. As can be seen from Figures 1g and 2a, Cu, O and S all existed in the samples. Simultaneously, the powder X-ray diffraction (XRD) pattern of CCS exhibited both the characteristic peaks of Cu_2O (JCPDS card No. 78-2076) and $Cu_{2-x}S$ (JCPDS No. 02-1292) (**Figure** 2b).[56,57] All these results confirmed the successful fabrication of CCS heterostructures.

Subsequently, the surface element valence and chemical composition of the as-prepared CCS heterostructures and Cu_2O were compared by X-ray photoelectron spectroscopy (XPS). Specifically, the characteristic peaks of S were only detected in the XPS spectra of CCS when compared with that of Cu_2O, which can also serve as a proof of the successful fabrication of CCS (Figure 2c).

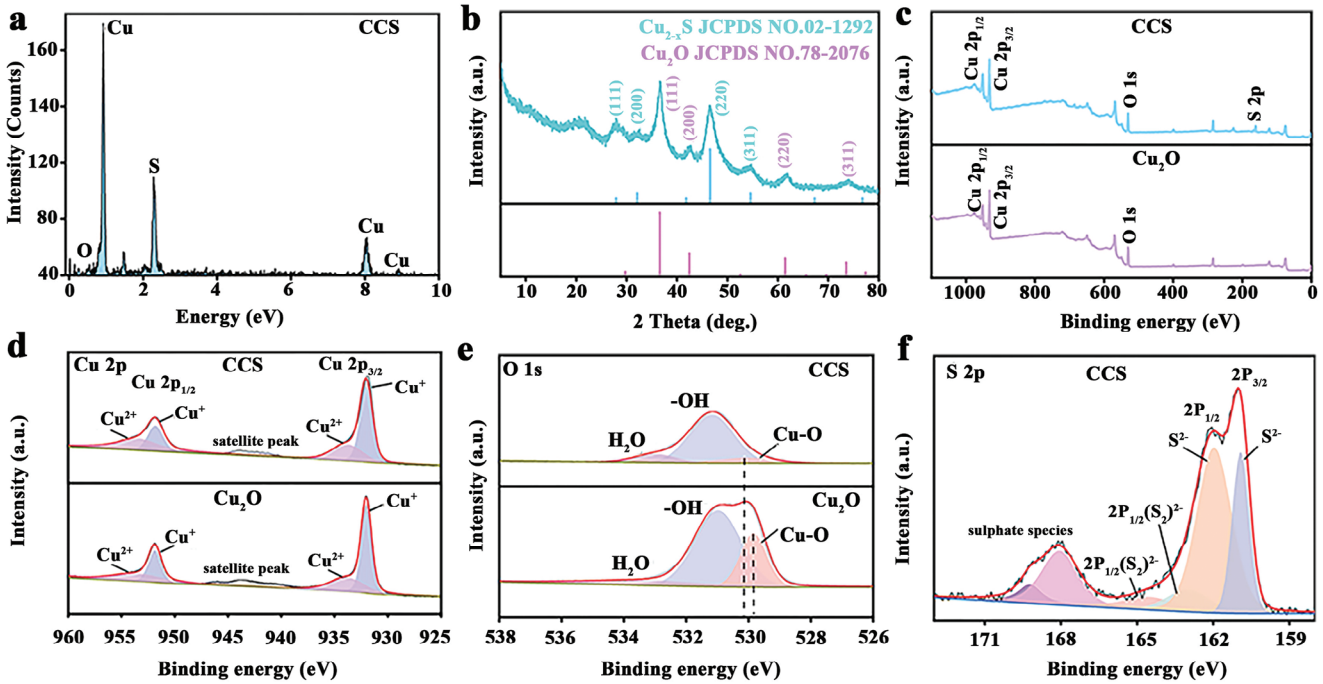

Figure 2. a) EDS spectrum of CCS NPs. b) XRD patterns of CCS NPs. c) Full XPS spectra for Cu_2O and CCS. d) Corresponding high-resolution spectra of Cu_2O and CCS for Cu 2p, e) O 1s and f) S 2p.

Compared with pure Cu_2O, the peak intensity of Cu(II) in CCS was significantly enhanced after the addition of sulfur source, which was consistent with the results of XRD patterns and could be attributed to the formation of $Cu_{2-x}S$ (Figure 2d). In the high-resolution O 1s spectrum of Cu_2O, there were three characteristic peaks at 529.8, 531.1, and 533.2 eV, which belong to lattice oxygen (Cu—O bond), —OH group and H_2O adsorbed on the surface, respectively (Figure 2e).[58] In comparison, the peak intensity of Cu—O at 529.8 eV in the spectrum of CCS was weaker than that of Cu_2O, which may be ascribed to the substitution of O by S to form the Cu—S bond.[59] The partial loss of O made the peak of Cu–O shift from 529.8 eV to the higher binding energy of 530.2 eV. The content of —OH in $Cu_2O/Cu_{2-x}S$ was higher than that in Cu_2O, therefore, it is beneficial to produce hydroxyl radicals in the process of photocatalytic reaction.[60] For the high resolution XPS spectrum of S 2p (Figure 2f), the peaks at 160.9 and 161.9 eV are indicative of S $2p_{3/2}$ and S $2p_{1/2}$, respectively, which are belong to S^{2-} species in Cu—S bond.[61] In addition, the appearance of the peaks at 163.1 and 164.6 eV correspond to the S—S bond,[62] and the peaks at ≈168.1 and 169.3 eV due to sulphate species is probably caused by the oxidation of S^{2-} during the ion exchange process.[63] These results demonstrate that there is an effective heterojunction structure between Cu_2O and $Cu_{2-x}S$, rather than a simple physical mixed phase, which is consistent with the TEM observation.

In order to endow the designed system with mild PTT therapeutic effect and the targeting property toward tumor cells, GA and HA were introduced into the CCS heterostructures. To achieve the effective loading of GA and HA, 2-aminoethanethiol was first modified on the surface of CCS. To simplify the expression, CCS modified with 2-aminoethanethiol is also abbreviated to CCS in the following. The amino groups of 2-aminoethanethiol changed the surface zeta potential of CCS to a positive charge (Figure S3a, Supporting Information), which was beneficial to the loading of GA and modification of HA through corresponding interaction. The effective modification of GA and HA was demonstrated by the characteristic peaks in Fourier transform infrared spectroscopy (FT-IR). For CCS@GA@HA, the adsorption bands of C—H group at 2972 cm^{-1} and aromatic rings (C=C) at 1444 cm^{-1} indicate the presence of GA. And the peak at 1043 cm^{-1} in the spectrum can be attributed to the C—O stretching vibration of the carboxyl group in HA (Figure S3b, Supporting Information). The loading amount of GA was calculated as 344.2 μg mg^{-1} according to a standard curve generated from the UV–vis spectrum at 360 nm of free GA at different concentrations (Figure S3c,d, Supporting Information). Such a high loading of GA was in favor of the mild PTT. The hydrodynamic size of the nanocomposite at different synthesis stages were measured by using dynamic light scattering (DLS). As shown in Figure S4 (Supporting Information)., the dynamic light scattering measurement results show that the sizes of CCS, CCS@GA and CCS@GA@HA were 56.13, 58.19, and 69.12 nm, respectively. Besides, DLS and digital photos (Figure S5, Supporting Information) also indicated that CCS@GA@HA can be stably incubated under various physiological conditions (DI water, PBS and RPMI 1640), and has potential biological application value.

2.2. Photothermal Properties of CCS Heterostructures

To investigate the photo-triggered performance, the absorption character of CCS was first detected. As shown in Figure S6 (Supporting Information), CCS showed an enhanced absorption

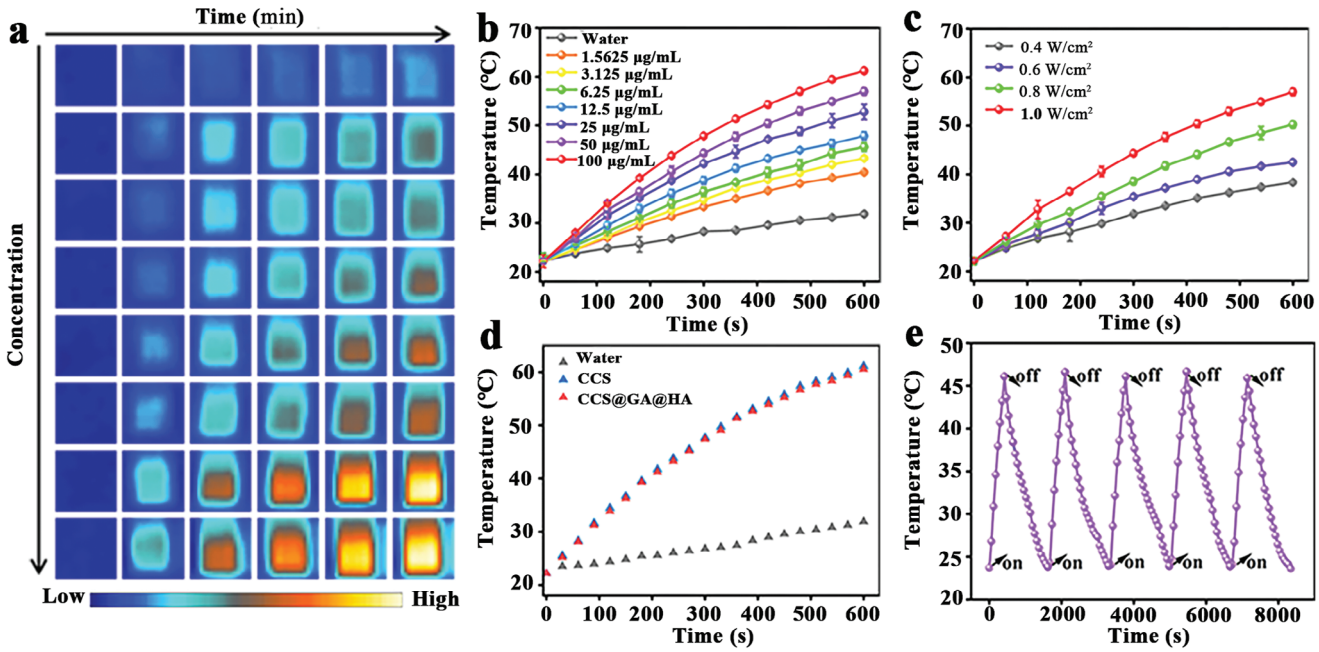

Figure 3. a) Infrared thermal images of CCS NPs aqueous solutions with elevated concentrations (0–100 μg mL^{-1}, 1.0 W cm^{-2}) under 1064 nm laser irradiation for 10 min. b) Temperature elevation curves of CCS NPs NPs aqueous solutions with different concentrations (0–100 μg mL^{-1}, 1.0 W cm^{-2}) under 1064 nm laser irradiation for 10 min. c) Temperature elevation curves of CCS NPs aqueous solutions (50 μg mL^{-1}) with various output power densities under 1064 nm laser irradiation. d) Temperature elevation activity comparison of water, CCS and CCS@GA@HA NPs aqueous solutions under 1064 nm laser irradiation for 10 min. e) Photothermal stability tests of CCS NPs (50 μg mL^{-1}) under NIR laser irradiation (1.0 W cm^{-2}).

in the NIR region, which is conducive to be used in the phototherapy. Then, the photothermal performance of CCS was evaluated and it also showed remarkable concentration and time-dependent property in the measured range (**Figure 3**a,b). Furthermore, the temperature changes of CCS NPs (50 μg mL^{-1}) with different laser power densities (0.4, 0.6, 0.8, 1.0 W cm^{-2}) was explored (Figure 3c; Figure S7, Supporting Information), the results showed that the photothermal effect of CCS was also power density dependent. The temperature of CCS (100 μg mL^{-1}) increased by 39 °C, which is much higher than that of deionized water (9.7 °C) after 1064 nm laser irradiation (1.0 W cm^{-2}) for 10 min (Figure S8, Supporting Information). The corresponding photothermal conversion efficiency (η) of CCS was calculated to be 36.6% by the fitted cooling curve, which was significantly higher than that of the commercial photothermal agent ICG (3.1%).[64] (Figure S9 and Table S1, Supporting Information). In order to determine the possible influence of GA and HA on the photothermal performance, the photothermal effect of the final nanocomposite CCS@GA@HA was also evaluated. It can be seen that the modification of GA and HA had almost no adverse impact on the photothermal performance when compared with CCS (Figure 3d). Additionally, the photothermal stability of CCS was evaluated by the repeated heating and cooling cycles. The changes of absorption in NIR and the attenuation on temperature variation of CCS can be ignored after five cycles (Figure 3e; Figure S10, Supporting Information). In addition, the morphology and the degradation ability of CCS also have no obvious changes during the treatment (Figure S11, Supporting Information). The above results illustrated the excellent structural and functional stability of the CCS heterostructure. All these results confirmed that CCS heterostructure had excellent photothermal performance and stability under a NIR II laser irradiation for potential PTT application.

2.3. Photocatalytic Performances and Mechanism of CCS Heterostructure

To clarify the photocatalytic performance and the corresponding mechanism, the energy band structure of CCS heterostructure was studied first. As can been seen in the UV–vis diffuse reflectance spectra of CCS, Cu_2O and $Cu_{2-x}S$ (**Figure 4**a), the existence of $Cu_{2-x}S$ endowed CCS with excellent absorption capacity in the NIR-II region, which made it possible to improve the tissue penetrability and biosafety by choosing a NIR-II laser as the light source of phototherapy.[65] Tauc plots used for optical-band-gap determination of CCS, Cu_2O, and $Cu_{2-x}S$ are shown in Figure 4b. According to the equation, $(Rh\nu)^n = A(h\nu\text{-}E_g)$,[66] the band gap ($E_g$) of CCS, Cu_2O and $Cu_{2-x}S$ are calculated as 1.87, 2.50, and 1.31 eV, respectively. Compared with Cu_2O, the band gap is significantly reduced after the formation of CCS heterojunction, which may give a reasonable explanation to the effective activation of CCS by NIR-II laser irradiation during the PCT. Meanwhile, the band gap of CCS was broadened compared with $Cu_{2-x}S$, which helped to improve the separation efficiency of charge carriers and enhance the photocatalytic performance. According to the valence band XPS spectra, the valence band potentials (E_{VB}) of CCS, Cu_2O, and $Cu_{2-x}S$ were determined as 1.21, 0.93, and 1.07 eV, respectively (Figure 4c). The conduction band potentials (E_{CB}) of CCS, Cu_2O, and $Cu_{2-x}S$ were calculated

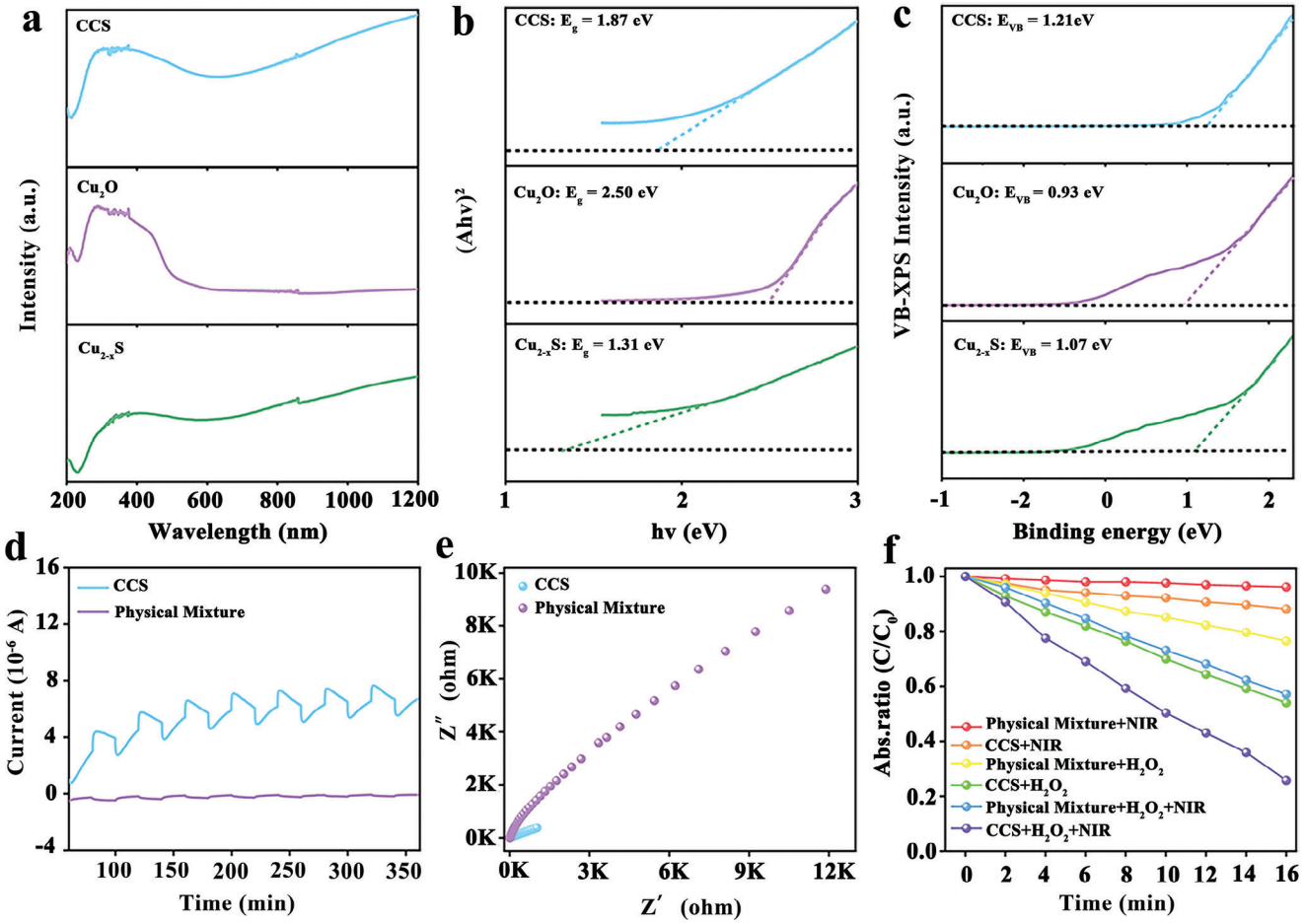

Figure 4. a) UV–vis diffuse reflectance spectra (UV–vis DRS) of CCS, Cu_2O and $Cu_{2-x}S$. b) Tauc plot for optical-band-gap determination of CCS, Cu_2O, and $Cu_{2-x}S$. c) Valence band XPS spectra of CCS, Cu_2O, and $Cu_{2-x}S$. d) Transient photocurrent responses of CCS NPs and physical mixture. e) Electrochemical impedance spectra (EIS) of CCS NPs and physical mixture. f) The UV/vis absorption decay ratio of DPBF fluorescence (C/C_0) after being treated with physical mixture, CCS with H_2O_2, and NIR irradiation under different conditions.

as −0.66, −1.57, and −0.24 eV, respectively, by the equation, $E_{CB} = E_{VB} - E_g$.[67] The photocatalytic mechanisms basing on the constructed energy band positions was discussed in the following section.

Then, the separation and transfer efficiency of photogenerated charge carriers in CCS heterostructures were investigated by transient photocurrent responses (TPR) and electrochemical impedance spectroscopy (EIS) tests. The physical mixture of Cu_2O and $Cu_{2-x}S$ was chosen as the control group. As shown in Figure 4d, the physical mixture group just exhibited negligible photocurrent while there was a strong response in the CCS heterostructures. Accordingly, the arc radius of CCS heterostructures was obviously smaller than that of the physical mixture group (Figure 4e). All these results confirmed that the formation of CCS heterojunction improved the separation and migration of photogenerated carriers efficiently, which was crucial to the enhancement of photocatalytic performance.

The photocatalytic performance of CCS heterostructures was preliminary evaluated by the generation of ROS using 1,3-diphenylisophenyl-furofuran (DPBF) as the probe. The experiments were carried out under three different conditions after considering the influences of H_2O_2 and NIR irradiation. As shown in Figure 4f and Figure S12 (Supporting Information), CCS and the physical mixture group just showed weak photocatalytic property in producing ROS under the NIR irradiation. In comparison, there was a more obvious decrease of the DPBF absorbance in the presence of H_2O_2, which could be attributed to the Fenton-like activity of the samples.[68] More importantly, under the combined treatment of NIR irradiation and H_2O_2, the absorbance of DPBF decreased sharply, indicating that the existence of NIR and H_2O_2 can make an explosion of ROS. It should be noted that, compared with the physical mixing group, CCS had showed the more excellent efficacy in ROS generation under the same condition, which confirmed the distinct advantages of the fabrication of CCS heterostructures.

Subsequently, electron spin resonance (ESR) spectroscopy was used to explore the mechanism of the ROS generation by CCS heterostructures. The physical mixture of Cu_2O and $Cu_{2-x}S$ was also chosen as the control group. As shown in **Figure 5a**, CCS + H_2O_2 had already showed a strong ·OH signal without NIR irradiation, which can be ascribed to the excellent Fenton-like activity of

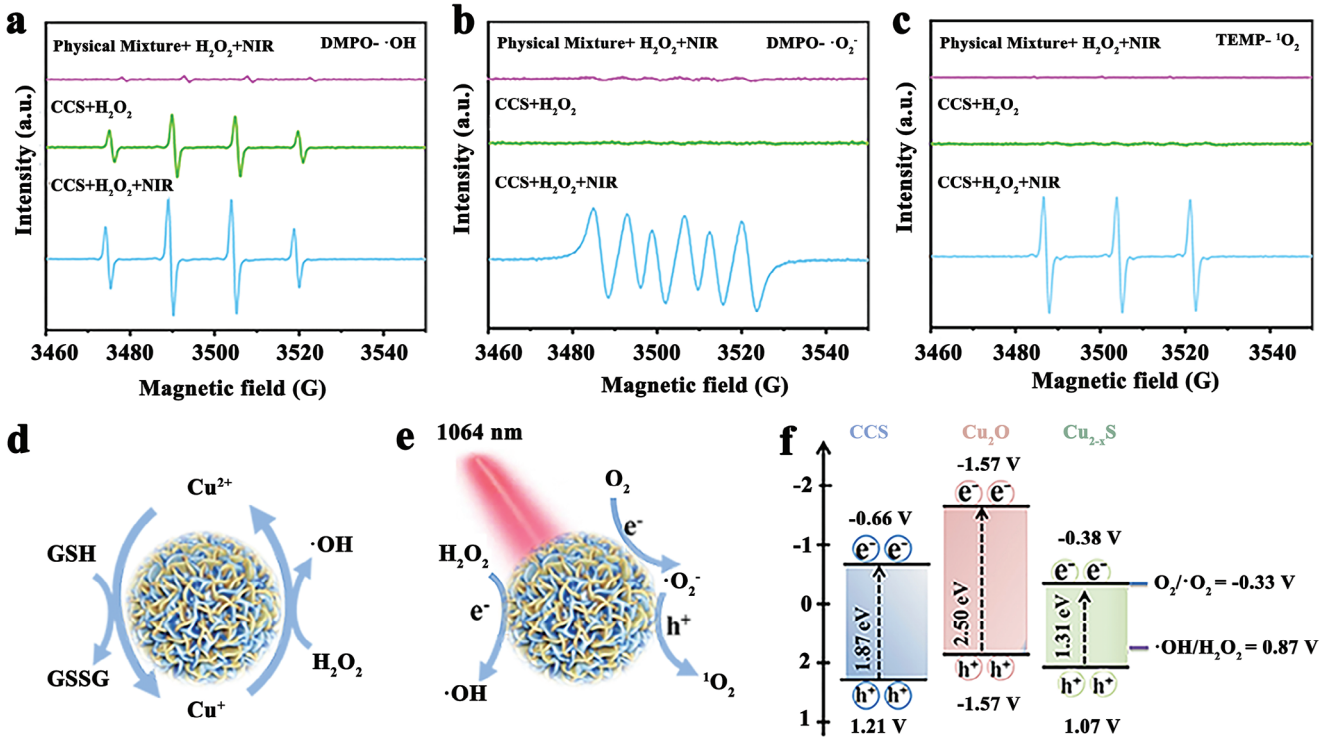

Figure 5. ESR spectra of a) DMPO/·OH, b) DMPO/$\cdot O_2^-$ and c) TEMP/$^1O_2$ treated with physical mixture and CCS under different conditions. d) Diagram of redox cycle reaction of GSH and ·OH conversion in CCS, e) Photocatalytic mechanism of CCS heterostructure under 1064 nm laser irradiation. f) The band structures of CCS, Cu_2O, and $Cu_{2-x}S$ and the energy positions of $\cdot OH/H_2O_2$ and $\cdot O_2^-/^1O_2$ formation processes.

CCS. And there was an obvious enhancement of ·OH signal after it was treated with NIR irradiation. Two possible reasons may explain this change. One was that the increasing temperature from the photothermal property of CCS accelerated the Fenton-like reaction to produce more ·OH. While the proper band structure of CCS may also provide another way to produce ·OH according to a photocatalytic process. At the same time, strong characteristic peaks of $\cdot O_2^-$ and $^1O_2$ appeared in the CCS + H_2O_2 group only after NIR irradiation (Figure 5b,c), indicating the good photocatalytic activity of CCS. Overall, CCS were more likely to produce abundant ROS than physical mixing, which can be derived from the superposition of multiple factors because of the existence of heterostructure. At the moment, the mechanism of the CCS producing ROS was almost clear. On the one hand, the Fenton-like activity of CCS resulted in the consumption of GSH and the production of ·OH (Figure 5d) according to the Cu^{2+}/Cu^+ redox cycle reaction. On the other hand, the proper heterostructure endowed CCS with efficient photocatalytic activity to produce ROS under NIR irradiation (Figure 5e). The matched energy level and improved separation efficiency of charge carriers had made CCS to produce ROS under NIR irradiation efficiently (Figure 5f).

2.4. Fenton-Like Reaction Activity and GSH Consumption of CCS NPs

It was well known that, as a typical Fenton-like catalyst, Cu^+ oxidized to Cu^{2+} by H_2O_2 can produce the highly toxic hydroxyl radicals (·OH). In this section, the Fenton-like reaction activity of CCS heterostructures was evaluated by the TMB oxidation tests.[69] As shown in Figure S13 (Supporting Information), in the simulated slightly acidic TME (pH 5.5) supplemented with H_2O_2, CCS group showed the typical absorption peak of oxidized TMB at 652 nm. In order to explore the impact of increased temperature on the Fenton-like reaction, the same group was maintained at 43 °C to simulate the optimal temperature of mild PTT. It can be seen that there was a significant increase in the absorption peak, which proved that heating-up really helped to enhance the Fenton-like catalytic activity of CCS. It is worth noting that the CCS group exhibits the strongest absorption under NIR irradiation, which can be attributed to the ingeniously designed heterostructures. For one thing, the excellent photothermal properties of CCS heterostructures can effectively heat up the catalyst to accelerate the Fenton-like reaction. For another, the photocatalytic property of CCS heterostructures has also resulted in the massive production of ROS. All these factors have jointly promoted the performance of the CCS group with NIR irradiation. In addition, all groups under neutral conditions (pH 7.4) were tested as control at the same time (Figure S14, Supporting Information). In sharp contrast to the acidic condition, the typical absorption was very weak in all groups, indicating the excellent selective response of CCS heterostructures to the TME.

Considering the potential to consume GSH due to the existence of Cu^{2+},[70] the ability of CCS to regulate GSH consumption was studied by using 5,5′-dithiobis-(2-nitrobenzoic acid) (DTNB) as the probe. As shown in Figure S15 (Supporting

Information), the absorption peak of DTNB at 412 nm drastically decreased with the increase of time, indicating the direct consumption of GSH by CCS. In order to further verify the reaction between GSH and CCS, the state changes of Cu^{+} and Cu^{2+} in CCS during the reaction were studied by XPS. The satellite peak of Cu^{2+} was significantly weakened, while the ratio of peak areas of Cu^{+}/Cu^{2+} increased (Figure S16a-c, Supporting Information), indicating that Cu^{2+} in CCS NPs was reduced to Cu^{+} through the reaction with GSH. Cu^{2+}-mediated GSH depletion and Cu^{+}-mediated Fenton-like reaction follow the following equation:

$$Cu^{+} + H_2O_2 \rightarrow Cu^{2+} + \cdot OH + OH^{-} \quad (1)$$

$$Cu^{2+} + GSH \rightarrow Cu^{+} + GSSG + H^{+} \quad (2)$$

2.5. Cytotoxicity and Anticancer Effects Evaluation In Vitro

Due to the strong ROS generation ability and excellent photothermal performance under NIR irradiation, then we studied the in vitro therapeutic effect of CCS@GA@HA. Considering the importance of biocompatibility in cancer treatment, the hemolysis test was first investigated to evaluate the biosafety of the samples (Figure S17, Supporting Information). After incubation with red-blood-cells (RBCs) for 4 h, the hemolysis rates of the samples were lower than 2.2% with different concentrations, indicating that the samples can be injected through vein with high safety. Before evaluating the anti-tumor effect in vitro, the cellular uptake capacity of different samples are tested first. The biological TEM images visually show the uptake behavior of CCS@GA and CCS@GA@HA. It can be observed that NPs are located in 4T1 cells. It is worthnote that the modification of HA on the surface of CCS@GA has made it more conducive to the effective endocytosis by cells. Flow cytometry analysis further prove that hyaluronic acid can indeed enhance cell uptake of nanodrugs. On the basis of the above experiments, the total copper content in 4T1 cells treated with CCS@GA and CCS@GA@HA was determined by ICP-MS, respectively. The results showed that the content of copper in CCS@GA@HA-treated cells (11.10 pg per 10 000 cells) was 1.9 times that of CCS@GA-treated 4T1 cells (5.95 pg per 10 000 cells.) (Figure S18, Supporting Information). These findings suggest that CCS@GA@HA can be efficiently accumulated by tumor cells.

Subsequently, the cytotoxicity of CCS@GA@HA was evaluated by the resin azure method.[71] After incubation with BRL-3A (a normal cell line) for 24 h, there just was a negligible influence on the growth of normal cells, even at a high concentration of 12.5 μg mL^{-1} after 24 h (Figure S19, Supporting Information). Similarly, the viability of 4T1 cells treated with different samples without NIR irradiation only decreased slightly when achieved a high dose treatment (**Figure 6a**), which can be attributed to the function of ·OH produced by the Cu^{+}/Cu^{2+}-mediated CDT reaction. In view of this, CDT alone in this system appeared to have a weak tumor suppression effect. However, after the NIR irradiation was intervened, there was a sharp decrease in the cell viability along with the sample concentration increased (Figure 6b). Among those groups, the cell viability of CCS+NIR group decreased to 40% (12.5 μg mL^{-1}), which could be attributed to the synergistic effect of PCT, PTT, and CDT modalities that had been discussed in CCS. After adding GA, the cell viability of CCS@GA group sharply decreased to 23% (12.5 μg mL^{-1}). It may be explained by the fact that GA can effectively inhibit the activity of HSP90 in tumor cells and reduced the heat resistance of tumor cells, which can greatly improve the photothermal therapeutic effect.[72] Meanwhile, the CCS@GA@HA+NIR group exhibited the lowest cell viability (8.7%), and this may be due to the function of HA which can help to enhance the tumor recognition and accumulation by binding to CD44 receptors on tumor cells.[73] All of these results suggest that this ingeniously designed system could greatly improve the therapeutic efficacy on tumor cells according to the synergistic effect of multiple modes.

To provide a visual feedback of the ROS generation in cells, 2′,7′-dichlorofluorescein diacetate (DCFH-DA) was chosen as the intracellular ROS probe, which exhibited the green fluorescence after being oxidized to 2′,7′-dichlorofluorescein (DCF) by the intracellular ROS.[74] As shown in Figure 6c,d, no obvious fluorescence enhancement was observed in CCS and CCS@GA@HA groups in comparison with the control group. However, there were great increase of the fluorescence intensity upon NIR laser irradiation. It is worth noting that the modification of GA and HA can both significantly improve the generation of ROS, and the reason was consistent with the analysis discussed above. Strong ROS production and efficient GSH consumption might lead to lipid peroxidation (LPO) and inactivate GPX4, thereby inducing ferroptosis in tumor cells. Next, we use the fluorescent probe Liperfluo to evaluate the LPO level in 4T1 cells. As expected, the fluorescence intensities of the groups were enhanced after NIR-II laser irradiation, and the CCS@GA@HA+NIR group showed the highest degree of green fluorescence, indicating the effective accumulation of LPO in 4T1 tumor cells (Figure 6e). Western blot results showed that the expression of GSH-related GPX4 in tumor cells was significantly down-regulated after treatment with CCS@GA@HA+NIR (Figure S20, Supporting Information).

It is well known that ferroptosis can cause mitochondrial oxidative damage, resulting in loss of membrane potential. JC-1 staining was used to monitor mitochondrial dysfunction. As shown in Figure 6f, compared with the non-laser irradiation group, the red fluorescence signal in the CCS+NIR and CCS@GA+NIR groups decreased and the green fluorescence enhanced to a certain extent, suggesting mitochondrial damage. In the CCS@GA@HA+NIR group, red fluorescence was negligible, indicating the greatest mitochondrial damage. In order to visualize the mitochondrial damage of 4T1 tumor cells, Bio-TEM experiments were performed on 4T1 cells treated with CCS@GA@HA+NIR and PBS, respectively. Compared with the PBS group, 4T1 cells treated with CCS@GA@HA+NIR showed obvious mitochondrial damage, manifested as smaller mitochondria, disappearance of mitochondrial cristae, and rupture of mitochondrial outer membrane (Figure S21, Supporting Information). The above findings suggest that the CCS@GA@HA+NIR can produce abundant ROS, resulting high levels of oxidative stress and consuming GSH to trigger ferroptosis in tumor cells. In addition, the results of living/dead cell staining experiments and flow cytometry analysis further confirmed the synergistic effect of this designed system (Figure 6g,h),

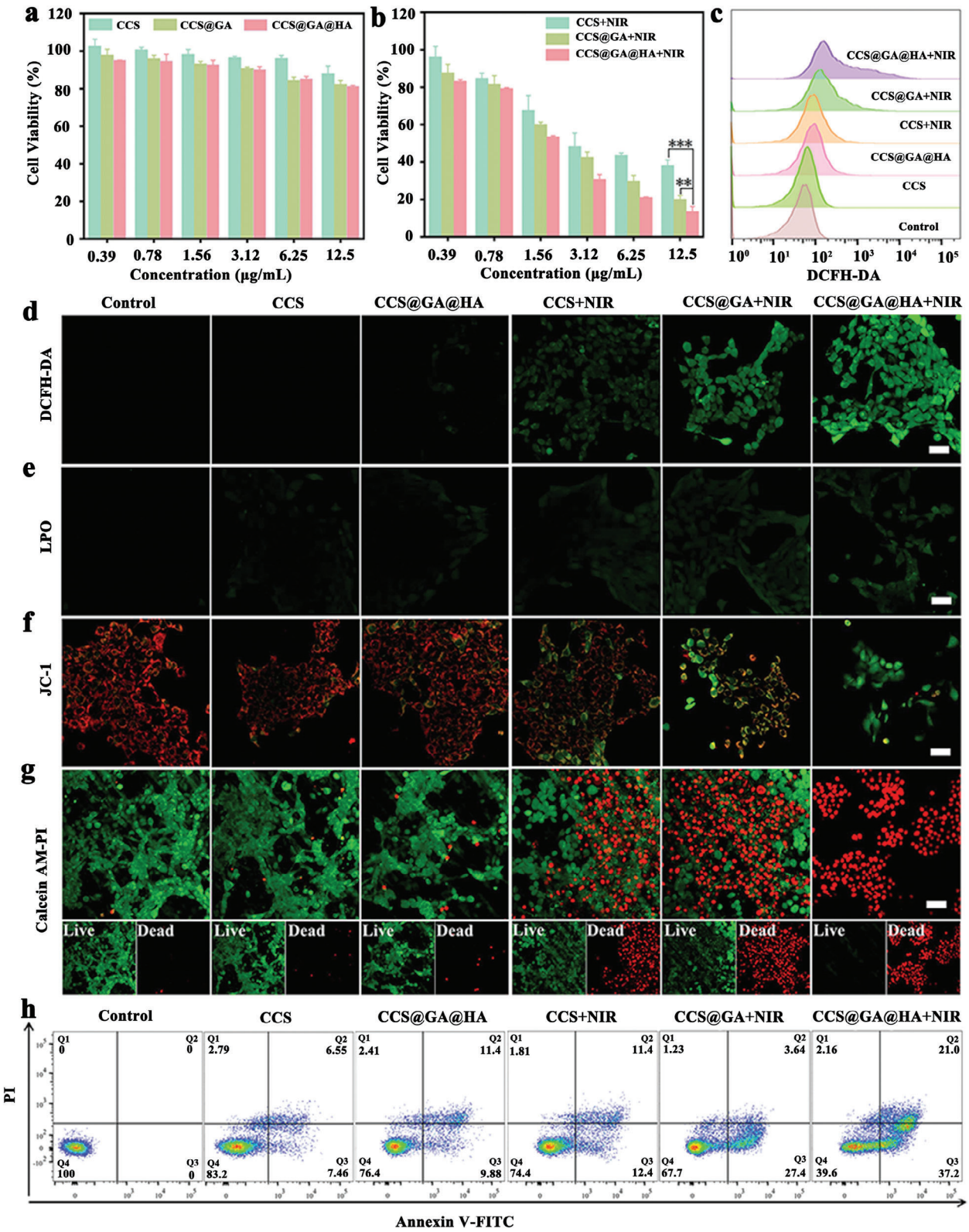

Figure 6. Cell viability of 4T1 cells incubated with CCS, CCS@GA, CCS@GA@HA with different concentrations without a) and with b) NIR laser irradiation (1064 nm, 1.0 W cm^{-2}). c) Fluorescence distributions of DCF showing ROS levels in 4T1 cells after various treatments measured by flow cytometry. d) CLSM images of 4T1 cells stained with DCFH-DA, e) LPO, and f) JC-1 after various treatments. g) Live/dead assays and h) flow cytometry detection of 4T1 cells with various treatments. Scale bar: 50 μm.

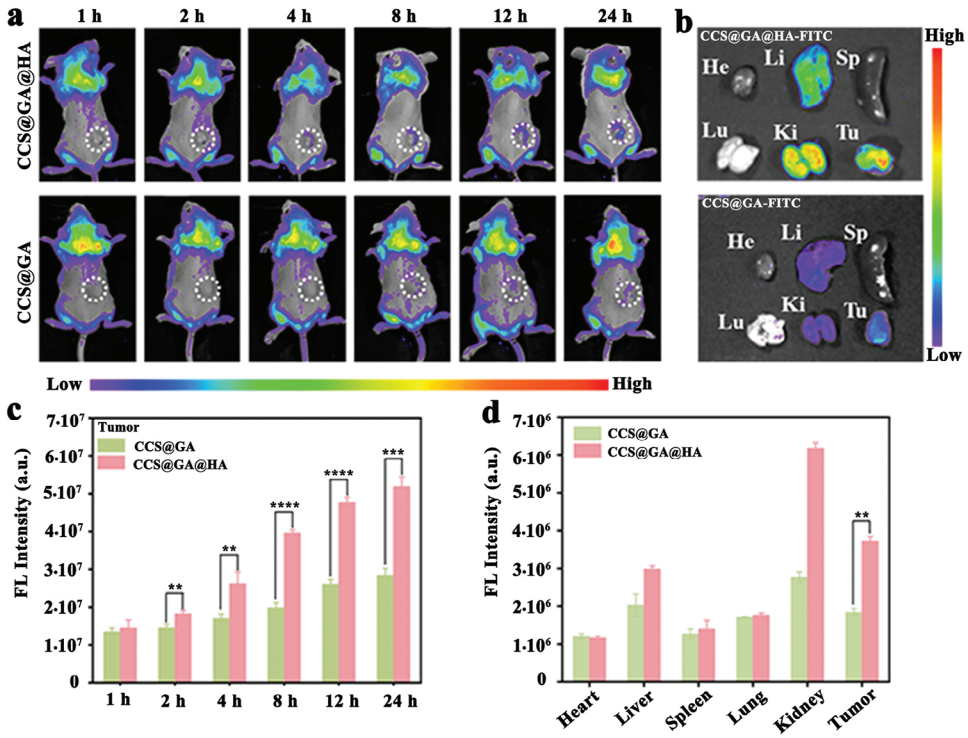

Figure 7. a) Fluorescence images of 4T1 tumor-bearing mice following intravenous administration of CCS@GA@HA and CCS@GA NPs labeled by FITC at various time points. b) Ex vivo fluorescence images of major organs and tumors after post injection of CCS@GA@HA and CCS@GA NPs. The corresponding quantitative analysis of fluorescence intensity of c) tumor sites in vivo and d) ex vivo main organs and tumors (n = 3).

which have an excellent therapeutic efficacy under NIR-II laser irradiation.

2.6. In Vivo Fluorescence Imaging

Encouraged by the results of in vitro treatment, 4T1 tumor-bearing mice were used as a model to explore the in vivo anticancer activity of CCS@GA@HA. In order to further confirm the targeting ability of CCS@GA@HA for tumor in vivo, a real-time fluorescence imaging system was first used to monitor the biodistribution of samples after intravenous administration. As shown in **Figure** 7a,c, the mice treated with CCS@GA@HA group showed a faster increase of fluorescence intensity in the tumor area within 24 h, while the CCS@GA group maintained a relatively low increasing rate. And the signal intensity of CCS@GA@HA group at 24 h post-injection was ≈1.8 times that of CCS@GA group, which further confirmed the effective accumulation of CCS@GA@HA in the tumor area. At the end of the experiment, the tumor and main organs (heart, liver, spleen, lung, kidney) were dissected for fluorescence imaging (Figure 7b,d). The fluorescence intensity of liver and kidney were the strongest in both groups, which can be explained by the fact that liver and kidney were the main organs for the metabolism and clearance of most NPs. Interestingly, the fluorescence intensity of tumor tissue in the CCS@GA@HA group was much higher than that in the CCS@GA group. These data further confirmed that CCS@GA@HA NPs can effectively target tumors and improve the in vivo performance, thereby overcoming the rapid clearance of drugs and promoting better therapeutic effects.

2.7. In Vivo Antitumor Efficacy and Toxicity Evaluation

In consideration of the satisfactory results in the above experiments, the 4T1 tumor-bearing mouse model was further used to evaluate the anti-tumor efficacy of CCS@GA@HA NPs-mediated synergistic multimodal therapy in vivo. We conducted in vivo experiments with six different treatment models, including group 1: PBS+NIR, group 2: CCS, group 3: CCS@GA@HA, group 4: CCS+NIR, group 5: CCS@GA+NIR, group 6: CCS@GA@HA+NIR, and then subjected to the corresponding treatments. The in vivo photothermal performance of different groups were first investigated. As shown in **Figure** 8a,b, the tumor temperature in the group treated with CCS@GA@HA rapidly increased to ≈43 °C after a 10 min NIR-II laser irradiation and maintained at this temperature, however, the temperature fluctuation of the tumor site in other NIR groups did not change much, indicating that the targeting effect of HA contributed to the effective accumulation of drugs at the tumor sites. The tumor volumes of each group were measured every other day and the tumor were collected after 18 days of treatment (Figure 8c; Figure S22, Supporting Information). Compared with the PBS treatment group, the samples without laser irradiation had less effect on inhibiting tumor growth. In contrast, it exhibited obvious inhibition of the tumor growth in the laser irradiation groups. More importantly, the tumor growth in the

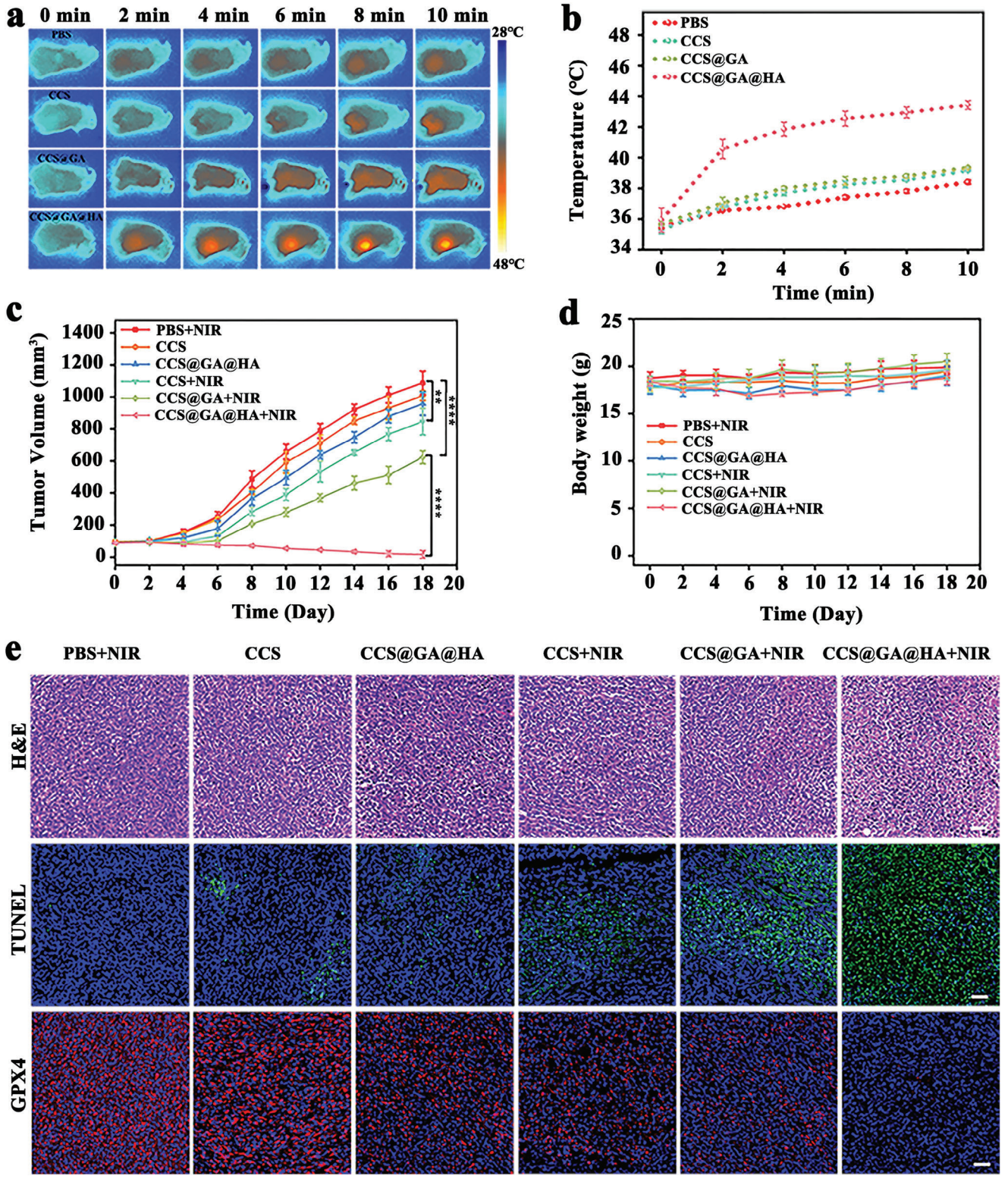

Figure 8. a) Time-dependent in vivo photothermal imaging pictures of 4T1 tumor-bearing mice after intravenous administration with different treatment under 1064 nm laser irradiation. b) Temperature curves of tumor region in different treatment groups. c) Tumor growth curves in different treatment groups and d) body weight changes of mice in different treatment groups. e) H&E staining images, TUNEL staining images and the corresponding GPX4 staining images of tumor tissues in different treatment groups. Scale bar: 50 μm.

CCS@GA@HA group with laser irradiation was almost completely inhibited. This designed system showed excellent antitumor ability in vivo.

In order to further evaluate the inhibitory of HSP90 overexpression induced by GA in vivo, the levels of HSP90 in tumor tissues were analyzed by fluorescence staining section technique (Figure S23, Supporting Information). Compared with the PBS group, CCS+NIR group showed the brightest green fluorescence, indicating that the rapid activation of HSP90 induced by photothermal effect led to the up-regulation of HSP90 expression in tumor tissues. However, the fluorescence intensity of tumors treated with CCS@GA was significantly reduced, which indicated that the expression of HSP90 decreased. This may be due to the introduction of GA which reduced the expression of HSP90. But most importantly, the CCS@GA@HA+NIR group exhibited the weakest green fluorescence because of the modification of HA which enhanced the aggregation of nanomaterials in the tumor area. The above results confirmed that the presence of GA can significantly inhibit the activity of HSP90, reduce the resistance of tumor cells to thermal ablation, and efficiently endow the mild photothermal therapeutic effect with CCS. In addition, tumor cell apoptosis and ferroptosis was evaluated by hematoxylin and eosin (H&E) staining, terminal deoxynucleotidyl transferase dUTP nick end labeling (TUNEL) and GPX4 (Figure 8e). As expected, CCS@GA@HA+NIR group showed the most severe tumor cell damage, such as increased cytoplasm, concentrated nucleus, and cell morphological changes, while the tumor cells in remaining groups were not significantly affected or partially damaged. TUNEL results were consistent with the above results. Moreover, immunofluorescence staining of tumor tissue sections showed that the expression of GPX4 in CCS@GA@HA+NIR group was the lowest, indicating the occurrence of ferroptosis in tumors. Negligible dead cells were observed in the main organs of all groups (Figure S24, Supporting Information), and it further confirmed the biocompatibility and specific selectivity of CCS@GA@HA to tumor tissues. Furthermore, there was no significant difference in all blood biochemical values between CCS@GA@HA + NIR treatment group and control mice, suggesting that CCS@GA@HA+NIR did not cause liver dysfunction and renal dysfunction, which also proved the good biosafety of CCS@GA@HA +NIR (Figure S25, Supporting Information).

3. Conclusion

In summary, an ingenious heterostructure (CCS@GA@HA) has been designed for the combination therapy of mild PTT, PCT, and CDT triggered by NIRII light simultaneously with infrared thermal imaging for anti-tumor therapy. Due to the existence of Cu^{+}/Cu^{2+}, CCS can work as a as a typical Fenton-like catalyst used for CDT. Through the simple fabrication of $Cu_{2-x}S$ on the surface of Cu_2O, CCS also exhibited a relatively high photothermal conversion efficiency (36.6%) under the NIR II light irradiation, and the loading of GA made it possible to perform the PTT under a low temperature. Meanwhile, the generated heat helped to accelerate Fenton reaction that eventually improved the CDT performance. Moreover, proper energy band structures of CCS endow it with promoted separation and transfer efficiency of photogenerated charge carriers to exhibit excellent PCT under NIRII light irradiation. Consequently, the efficient PCT combined with TME-activated GSH consumption and the accelerated CDT had made an explosion of ROS, which help achieve effective ferroptosis. The modification of HA not only increased the accumulation and uptake of samples by tumor cells, but also helped to avoid non-specific damage to normal cells, which were impressively justified by in vitro and in vivo surveys. Therefore, the facile fabrication of CCS@GA@HA has realized the combination therapy of NIR-triggered mild PTT, PCT, CDT and ferroptosis, providing an inspiration for the potential design and fabrication of nanoplatforms for multiple-mode synergistic tumor therapy.

4. Experimental Section

Materials: All chemicals and reagents were used without further purification. Polyvinylpyrrolidone (PVP, K40) was acquired from Shanghai Sangon Reagent Co., Ltd. Sodium hydroxide (NaOH) was obtained from Tianli Chemical Reagent Co., Ltd. Ascorbic acid (AA) was purchased from Damao Chemical Reagent Co., Ltd. Copper (II) chloride dihydrate ($CuCl_2{\cdot}2H_2O$) and thioacetamide (TAA) were purchased from Sinopharm Chemical Reagent Co., Ltd. 2-aminoethanethiol was purchased from EnergyChemical Chemical Reagent Co., Ltd. Hydrogen peroxide (H_2O_2, 30%) was purchased from Shanghai Deen Chemical Reagent Co., Ltd. Hyaluronic acid (HA) (molecular weight 40–100 KDa) and 3,3′,5,5′-tetramethylbenzidine (TMB) were supplied by Macklin Reagent Co., Ltd. Resazurin were purchased from Sigma–Aldrich. Calcein-AM/PI dual staining kit, ROS detection kit (DCFH-DA) and Annexin V-FITC apoptosis detection kit were purchased from Beyotime.

Instruments: Scanning electron microscopy (SEM) micrographs were recorded on SU8010 Field emission electron microscope (FE-SEM, Japan) and transmission electron microscope (TEM) analyses were performed using a JEM-2100 transmission electron microscope equipped with a selected-area electron diffraction (SAED). The crystalline structures of the prepared products were determined by the powder X-ray diffraction (XRD) on an X'Pert3 Powder in the 2θ range of 5–80° (PANalytical B.V., Holland). X-ray photoelectron spectroscopy (XPS) spectra were recorded on Escalab 250Xi, Thermo Scientific. The fourier transform infrared (FT-IR) spectra were recorded on a Perkin–Elmer 400 spectrophotometer with the KBr pellet technique. The UV–vis absorption spectra were measured on an Agilent Technologies Cary 100 UV–vis spectrophotometer. The zeta potential and hydrodynamic particle size of the samples were determined by a Zetasizer Nano ZS90 laser particle analyzer (Malven, USA). The cell assay experiments were performed in EnVision Multilabel Reader (PerkinElmer) system. In vivo fluorescence imaging (FLI) was detected by IVIS imaging system (LB983 NC100).

Synthesis of Cu_2O: Cu_2O nanoparticles were synthesized according to the reported method. Briefly, 0.5 mmol $CuCl_2{\cdot}2H_2O$ was first dissolved in 20 mL of water contained 0.6 g PVP under stirring for 30 min at room temperature. Then, NaOH aqueous solution (1 mL, 8 M) was added to the above mixture dropwise. After stirring for 10 min, AA aqueous solution (1 mL, 1 M) was slowly added to the above solution and stirred for another 10 min. The obtained Cu_2O-PVP nanoparticles (NPs) nanoparticles were collected by high speed centrifugation and washed with water several times.

Synthesis of $Cu_{2-x}S$: The as-prepared Cu_2O NPs were used as the template to prepare $Cu_{2-x}S$ NPs. First, the freshly prepared TAA solution was added into the aqueous suspension of the Cu_2O NPs and stirred for 1 h at room temperature. The obtained $Cu_{2-x}S$ NPs were collected through ultracentrifugation and washed with water for several times.

Preparation of CCS: The as-prepared Cu_2O NPs were used as the template to prepare $Cu_2O/Cu_{2-x}S$ NPs. First, the freshly prepared 1 M of TAA solution was added into the aqueous suspension of the Cu_2O NPs and stirred for 1 h at room temperature. The obtained $Cu_2O/Cu_{2-x}S$ NPs were collected through ultracentrifugation and washed with water for several times. Furthermore, 10 mg of $Cu_2O/Cu_{2-x}S$ was dissolved in 30 mL of

PBS and sonicated to form a homogeneous suspension, and 40 mg of 2-aminoethanethiol were added under strong stirring for 24 h to obtain $Cu_2O/Cu_{2-x}S$-NH_2 (CCS).

Preparation of Physical Mixture of Cu_2O and $Cu_{2-x}S$: The physical mixture of Cu_2O and $Cu_{2-x}S$ was prepared according to the stoichiometric ratio of Cu_2O and $Cu_{2-x}S$ in CCS.

Preparation of CCS@GA@HA: To obtain the CCS@GA@HA, GA (5 mg) was added to 5 mL CCS NPs suspension in methanol and stirred for 12 h in room temperature. Finally, the mixture was collected by centrifugation and washed several times with methanol to obtain the CCS@GA. The freshly prepared CCS@GA was dispersed in 5 mL HA solution (2 mg mL^{-1}) and stirred at room temperature for 12 h. Finally, the mixture was collected by centrifugation and washed several times with water to obtain the CCS@GA@HA.

In Vitro Photothermal Performance: To study the photothermal effect of CCS NPs, the CCS NPs solution with various concentrations (0, 1.5625, 3.125, 6.25, 12.5, 25, 50, 100 μg mL^{-1}) was irradiated by 1064 nm laser for 10 min at power density of 1 W cm^{-2} and the temperature of the solution at different time points were monitored by thermal imaging camera. At the same time, real-time thermal images at different time points were recorded.

Photothermal Effect and Photothermal Conversion Efficiency: To study the photothermal stability of CCS NPs. 1 mL of the CCS NPs solution with 50 μg mL^{-1} concentration was irradiated by 1064 nm laser for 7 min at power density of 1 W cm^{-2}, then the 1064 nm laser was turned off and the solution was naturally cooled to room temperature. This process was repeated with five light on/off cycles. Meanwhile, the above method was used to study the photothermal conversion efficiency. The sample was exposed to the 1064 nm laser for 19 min, and then turned off the laser to naturally cool to room temperature. The photothermal conversion efficiency (η) of CCS NPs can be calculated the following reported method.

$$\eta\ (\%) = \frac{hS\ (T_{Max} - T_{Surr}) - Q_{Dis}}{I\ \left(1 - 10^{-A_{1064}}\right)} \quad (3)$$

Where T_{max} and T_{surr} represents the maximum steady-state temperature of CCS NPs and environmental temperature, respectively. The Q_{dis} was heat loss caused by the vessel from light absorbed, I was the laser power density and A_{1064} was the absorbance of CCS NPs at 1064 nm. The hS was obtained according to the Equation (4):

$$hS = \frac{mDcD}{\tau S} \quad (4)$$

m_D and c_D were the quality and heat capacity (4.2 J g^{-1}) of the deionized water, respectively. The τs was the sample system time constant. According to the above equation, the η of the CCS NPs was calculated to 36.6%.

Chemodynamic Activity Evaluation of CCS@GA@HA NPs: The production of ·OH was detected by 3,3′,5,5′-Tetramethylbenzidine (TMB). CCS@GA@HA (400 μg mL^{-1}), TMB (40 μg mL^{-1}) and H_2O_2 (10 mM) were added into PBS with different pH values (pH 7.4 and pH 5.5), respectively, and then the solutions were stirred under dark at room temperature (25 °C) or 43 °C for 10 min. After that, the solutions were centrifuged and the absorbance at 652 nm was detected by UV–vis spectroscopy.

Hemolysis Test: The blood compatibility of CCS, CCS@GA, and CCS@GA@HA NPs were evaluated by hemolysis test. The Red blood cells (RBCs) were isolated from serum by centrifugation at 2000 rpm for 5 min, then washed several times by PBS at pH 7.4. Afterwards, 200 μL of diluted RBCs suspension was added to 800 μL of PBS with the addition of different concentrations of CCS, CCS@GA, and CCS@GA@HA NPs (0.39–50 μg mL^{-1}). All of the mixtures were incubated for 4 h at 37 °C, after that, the supernatant was collected by centrifugation at 12 000 rpm for 5 min and the absorbance at 570 nm of the supernatant was measured. The deionized water and PBS were served as positive and negative controls, respectively. The hemolysis rate was calculated by the following equation:

$$\text{Hemolysis ratio}\ (\%) = \frac{A\ (\text{sample},\ 570\ \text{nm}) - A\ (\text{negative},\ 570\ \text{nm})}{A\ (\text{positive},\ 570\ \text{nm}) - A\ (\text{negative},\ 570\ \text{nm})} \quad (5)$$

Cell Culture: The 4T1 and BRL-3A cells line were seeded in RPMI-1640 and DMEM medium supplemented with 10% (v/v) FBS, 1% (v/v) penicillin and 1% (v/v) streptomycin, respectively. All the cell lines were incubated at 37 °C in a humidified CO_2 atmosphere (5%) for 24 h.

In Vitro Biocompatibility and Cytotoxicity Analysis: The cell biocompatibility and cytotoxicity were assessed by using the resin azure assay. Briefly, BRL-3A cells or 4T1 cells (5×10^3 cells per well) were preseeded in 96-well microplates. The cells then were treated with different concentration (0, 0.39, 0.78, 1.56, 3.12, 6.25, and 12.5 μg mL^{-1}) of CCS, CCS@GA, and CCS@GA@HA NPs for 24 h. The fluorescence intensity of the supernatant was recorded (Ex = 540 nm, Em = 590 nm) after the Resazurin aqueous solution (20 μL, 0.5 mg mL^{-1}) was added and incubated for another 4 h. For cytotoxicity evaluation, the 4T1 cells treated with different concentration (0, 0.39, 0.78, 1.56, 3.12, 6.25, and 12.5 μg mL^{-1}) of CCS, CCS@GA and CCS@GA@HA NPs were dispersed in RPMI-1640 medium, respectively. After 24 h, the incubated 4T1 cells were irradiated by NIR (1 W cm^{-2} at 1064 nm) for 5 min and incubated for another 2 h. After another 4 h of incubation, the cytotoxicity was evaluated with the above standard Resazurin method.

Live/Dead Staining Assay: This was investigated by the Double Staining Kit calcein-AM and PI. 4T1 cells were inoculated on confocal dishes at 8×10^4 cells per dish overnight. Then the 4T1 cells were treated CCS, CCS@GA, and CCS@GA@HA NPs for 24 h, respectively, and the 4T1 cells were also treated with or without NIR. The cells were washed three times with PBS after incubated for another 4 h. Subsequently, the cells were stained with Double Staining Kit calcein-AM and PI for 20 min and then observed by confocal laser scanning microscopy (CLSM).

Cell Apoptosis Assessments Assay: 4T1 cells were seeded in six-well plates at a density of 1.2×10^5 cells per well and incubated at 37 °C overnight. After that, the 4T1 cells were incubated with CCS, CCS@GA, and CCS@GA@HA for 24 h. Then, the 4T1 cells were treated with and without NIR for 5 min, respectively. After incubated for another 4 h, all cells were collected and washed three times with cold PBS. Then, 10 μL of PI and 5 μL Annexin V-FITC were utilized to co-stain the cells for 15 min at 37 °C. At last, the cells were quantitatively monitored by flow cytometer.

Intracellular ROS Detection: ROS detection kit (2,7′-dichlorodihydrofluorescein diacetate (DCFH-DA) was used to evaluate the generation of ROS in cells. 4T1 cells were seeded in confocal dishes at a density of 7×10^4 cells and cultured for 24 h at 37 °C in 5% CO_2. After that, 4T1 cells were incubated with different samples (CCS, CCS@GA, CCS@GA@HA) for 6 h, respectively. Subsequently, 4T1 cells were washed twice with PBS and irradiated with NIR (1 W cm^{-2}) for 5 min, and the cells were incubated with DCFH-DA for 30 min, the cells were washed three times with PBS and observed by CLSM (Olympus, Model FV1200). Meanwhile, the cells were collected and analyzed by flow cytometry using the same method.

Tumor Model: The female athymic BALB/c mice (4–5 weeks old) were purchased from the Beijing Charles River Laboratory Animal Technology Co., Ltd. To develop the 4T1 breast tumor model, 150 μL phosphate-buffered saline with 4T1 cells (2×10^6) were subcutaneously injected into the right back side. When the 4T1-tumor-bearing mice of tumor volume was ≈100 mm^3, the in vivo therapy experiments of 4T1-tumor-bearing mice were carried out. Tumor diameters were measured with a digital caliper, and the tumor volume was calculated using the equation (mm^3) = (length × $width^2$)/2.

In Vivo and Ex Vivo Fluorescence Imaging: The 200 μL FITC-labeled CCS@GA NPs and CCS@GA@HA NPs were injected into tumor-bearing mice (n = 3) via the tail vein, respectively. Fluorescence imaging was performed using a fluorescence imaging system (IndiGo 2) at 1, 2, 4, 8, 12, and 24 h after injection, and the relative fluorescence imaging intensity of the tumor area was recorded. Tumor tissues and major organs were collected for ex vivo fluorescence imaging.

In Vivo Thermal Imaging and Mild-Temperature PTT Therapy: 4T1 tumor-bearing BALB/c mice were randomly divided into six groups (n = 5 mice per group): group 1: PBS+NIR, group 2: CCS, group 3: CCS@GA@HA, group 4: CCS+NIR, group 5: CCS@GA+NIR, group 6: CCS@GA@HA+NIR. These mice were intravenously injected with different samples at a dose of 15 mg kg^{-1} (200 μL), respectively. After 24 h,

the tumor region was irradiated with the NIR for 10 min (1.0 W cm^{-2}). At the same time, the laser irradiation group used a thermal imaging camera (FLIR E5) to continuously monitor the temperature and image of the tumor area at different time points every 2 min. During the treatment, the tumor size and body weight of each mice were recorded every two days. All the mice were euthanatized at day 18 of treatment, the tumors and major organs (heart, liver, spleen, lung, kidney) were also collected for further histological analysis by H&E staining and TUNEL staining. The treatment was initiated All animal procedures for this study were approved by the Academic Committee of Henan Normal University.

Statistical Analysis: All results were obtained from at least three replicates. All data were expressed as the mean ± standard deviation (S.D). Statistical evaluation was performed using one-way ANOVA or two-tailed independent t-test to detect group differences, with statistical significance established at $*p < 0.05$, $**p < 0.01$, $***p < 0.001$.

Supporting Information

Supporting Information is available from the Wiley Online Library or from the author.

Acknowledgements

This work was financially supported by the National Natural Science Foundation of China (21771058 and 21877027) and the Natural Science Foundation of Henan (212300410009 and 232300421302), the 111 Project (No. D17007), the Program for Science & Technology Innovation Talents in Universities of Henan Province (No. 23HASTIT002) and the Foundation of Henan Educational Committee (23A150021). Natural Science Foundation of Henan Province of China (Key Program, No. 242300421205). Key Science and Technology Project of Henan Province (232102310223).

Conflict of Interest

The authors declare no conflict of interest.

Data Availability Statement

The data that support the findings of this study are available in the supplementary material of this article.

Keywords

$Cu_2O/Cu_{2-x}S$ heterostructure, ferroptosis, multi-modal treatments, synergistic effect

Received: May 12, 2024
Revised: August 31, 2024
Published online:

[1] J. Li, T. Chen, *Coord. Chem. Rev.* **2020**, *418*, 213355.
[2] R. L. Siegel, K. D. Miller, H. E. Fuchs, A. Jemal, *Ca-Cancer J. Clin.* **2022**, *72*, 7.
[3] Y. Liu, P. Bhattarai, Z. Dai, X. Chen, *Chem. Soc. Rev.* **2019**, *48*, 2053.
[4] L. Cheng, C. Wang, L. Feng, K. Yang, Z. Liu, *Chem. Rev.* **2014**, *114*, 10869.
[5] Z. Pei, H. Lei, L. Cheng, *Chem. Soc. Rev.* **2023**, *52*, 2031.
[6] S. Dong, Y. Dong, Z. Zhao, J. Liu, S. Liu, L. Feng, F. He, S. Gai, Y. Xie, P. Yang, *J. Am. Chem. Soc.* **2023**, *145*, 9488.
[7] Y. Wang, X. Dai, C. Dong, W. Guo, Z. Xu, Y. Chen, H. Xiang, R. Zhang, *Adv. Mater.* **2022**, *34*, 2106773.
[8] Y. Li, R. Jia, H. Lin, X. Sun, F. Qu, *Adv. Funct. Mater.* **2021**, *31*, 2008420.
[9] Y. Pan, Y. Zhu, C. Xu, C. Pan, Y. Shi, J. Zou, Y. Li, X. Hu, B. Zhou, C. Zhao, Q. Gao, J. Zhang, A. Wu, X. Chen, J. Li, *ACS Nano* **2022**, *16*, 19038.
[10] L. Lin, S. Wang, H. Deng, W. Yang, L. Rao, R. Tian, Y. Liu, G. Yu, Z. Zhou, J. Song, H. Yang, Z. Chen, X. Chen, *J. Am. Chem. Soc.* **2020**, *142*, 15320.
[11] Y. Shao, B. Liu, Z. Di, G. Zhang, L. Sun, L. Li, C. Yan, *J. Am. Chem. Soc.* **2020**, *142*, 3939.
[12] J. Li, T. Chen, *Coord. Chem. Rev.* **2020**, *418*, 213355.
[13] X. Qu, F. Yin, M. Pei, Q. Chen, Y. Zhang, S. Lu, X. Zhang, Z. Liu, X. Li, H. Chen, Y. Zhang, H. Qin, *ACS Nano* **2023**, *17*, 11466.
[14] C. Xu, Y. Wang, E. Wang, N. Yan, S. Sheng, J. Chen, L. Lin, Z. Guo, H. Tian, X. Chen, *Adv. Funct. Mater.* **2021**, *31*, 2009314.
[15] F. Duan, X. Feng, X. Yang, W. Sun, Y. Jin, H. Liu, K. Ge, Z. Li, J. Zhang, *Biomaterials* **2017**, *122*, 23.
[16] J. Cheng, L. Li, D. Jin, Y. Dai, Y. Zhu, J. Zou, M. Liu, W. Yu, J. Yu, Y. Sun, X. Chen, Y. Liu, *Adv. Mater.* **2023**, *35*, 2210037.
[17] Q. Zhao, L. Zheng, Y. Gao, J. Li, J. Wei, M. Zhang, J. Sun, J. Ouyang, N. Na, *J. Am. Chem. Soc.* **2023**, *145*, 12586.
[18] D. Yan, M. Wang, Q. Wu, N. Niu, M. Li, R. Song, J. Rao, M. Kang, Z. Zhang, F. Zhou, D. Wang, B. Z. Tang, *Angew. Chem., Int. Ed.* **2022**, *61*, 202202614.
[19] F. Duan, Q. Jia, G. Liang, M. Wang, L. Zhu, K. J. McHugh, L. Jing, M. Du, Z. Zhang, *ACS Nano* **2023**, *17*, 11290.
[20] X. Ye, X. Liang, Q. Chen, Q. Miao, X. Chen, X. Zhang, L. Mei, *ACS Nano* **2019**, *13*, 2956.
[21] J. Dai, Y. Cheng, J. Wu, Q. Wang, W. Wang, J. Yang, Z. Zhao, X. Lou, F. Xia, S. Wang, B. Z. Tang, *ACS Nano* **2020**, *14*, 14698.
[22] B. Yang, Y. Chen, J. Shi, *Chem. Rev.* **2019**, *119*, 4881.
[23] Z. Li, C. Wang, C. Dai, R. Hu, L. Ding, W. Feng, H. Huang, Y. Wang, J. Bai, Y. Chen, *Biomaterials* **2022**, *287*, 121668.
[24] J. Liang, G. Luo, W. Chen, X. Zhang, *Adv. Mater.* **2021**, *33*, 2007630.
[25] F. Moradi Kashkooli, A. Jakhmola, T. K. Hornsby, J. Tavakkoli, M. C. Kolios, *J. Control Release* **2023**, *355*, 552.
[26] K. Chen, A. Zhou, X. Zhou, J. He, Y. Xu, X. Ning, *Sci. Adv.* **2024**, *10*, eadk3201.
[27] Y. Liu, R. Niu, R. Deng, Y. Wang, S. Song, H. Zhang, *Adv. Mater.* **2023**, *36*, 2307752.
[28] H. Zhu, C. Huang, J. Di, Z. Chang, K. Li, S. Zhang, X. Li, D. Wu, *ACS Nano* **2023**, *17*, 12544.
[29] L. Yang, Y. Zhu, L. Liang, C. Wang, X. Ning, X. Feng, *Nano Lett.* **2022**, *22*, 4207.
[30] J. Wang, Z. Fang, C. Zhao, Z. Sun, S. Gao, B. Zhang, D. Qiu, M. Yang, F. Sheng, S. Gao, Y. Hou, *Adv. Mater.* **2024**, *36*, 2307006.
[31] W. Fan, B. Yung, P. Huang, X. Chen, *Chem. Rev.* **2017**, *117*, 13566.
[32] L. Yuan, C. Zhang, Y. Zou, T. Bao, J. Wang, C. Tang, A. Du, C. Yu, C. Liu, *Adv. Funct. Mater.* **2023**, *33*, 2214627.
[33] X. Gao, J. Feng, K. Lv, Y. Zhou, R. Zhang, S. Song, H. Zhang, D. Wang, *Nano Res.* **2023**, *16*, 5322.
[34] Q. Bai, M. Liang, W. Wu, C. Zhang, X. Li, M. Liu, D. Yang, W. W. Yu, Q. Hu, L. Wang, F. Du, N. Sui, Z. Zhu, *Adv. Funct. Mater.* **2022**, *32*, 2112683.
[35] L. Chen, L. Zhou, C. Wang, Y. Han, Y. Lu, J. Liu, X. Hu, T. Yao, Y. Lin, S. Liang, S. Shi, C. Dong, *Adv. Mater.* **2019**, *31*, 1904997.
[36] W. Huang, L. He, Z. Zhang, S. Shi, T. Chen, *ACS Nano* **2021**, *15*, 20225.
[37] M. Rahmati, E. A. Silva, J. E. Reseland, C. A. Heyward, H. J. Haugen, *Chem. Soc. Rev.* **2020**, *49*, 5178.
[38] C. Pan, Z. Mao, X. Yuan, H. Zhang, L. Mei, X. Ji, *Adv. Sci.* **2022**, *9*, 2105747.

[39] H. Wen, Z. Zhang, M. Kang, H. Li, W. Xu, H. Guo, Y. Li, Y. Tan, Z. Wen, Q. Wu, J. Huang, L. Xi, K. Li, L. Wang, D. Wang, B. Z. Tang, *Biomaterials* **2021**, *274*, 120892.
[40] H. Wang, D. Jiao, D. Feng, Q. Liu, Y. Huang, J. Hou, D. Ding, W. Zhang, *Adv. Mater.* **2024**, *36*, 2311733.
[41] L. Zhang, M. Qiu, R. Wang, S. Li, X. Liu, Q. Xu, L. Xiao, Z.-X. Jiang, X. Zhou, S. Chen, *Angew. Chem., Int. Ed.* **2024**, *63*, 202403771.
[42] L. Wang, X. Zhang, Z. You, Z. Yang, M. Guo, J. Guo, H. Liu, X. Zhang, Z. Wang, A. Wang, Y. Lv, J. Zhang, X. Yu, J. Liu, C. Chen, *Angew. Chem., Int. Ed.* **2023**, *62*, 202217448.
[43] L. Wu, H. Lin, X. Cao, Q. Tong, F. Yang, Y. Miao, D. Ye, Q. Fan, *Angew. Chem., Int. Ed.* **2024**, *63*, 202405937.
[44] T. Yang, M. Zhou, M. Gao, W. Qin, Q. Wang, H. Peng, W. Yao, L. Qiao, X. He, *Small* **2023**, *19*, 2205692.
[45] W. Liu, Q. Chen, J. Wu, F. Zhang, L. Han, J. Liu, H. Zhang, Z. Hao, E. Shi, Y. Sun, R. Zhang, Y. Wang, L. Zhang, *Adv. Funct. Mater.* **2024**, *34*, 2312308.
[46] B. Tian, R. Tian, S. Liu, Y. Wang, S. Gai, Y. Xie, D. Yang, F. He, P. Yang, J. Lin, *Adv. Mater.* **2023**, *35*, 2304262.
[47] T. Hu, L. Yan, Z. Wang, W. Shen, R. Liang, D. Yan, M. Wei, *Chem. Sci.* **2021**, *12*, 2594.
[48] X. Wang, X. Zhong, H. Lei, Y. Geng, Q. Zhao, F. Gong, Z. Yang, Z. Dong, Z. Liu, L. Cheng, *Chem. Mater.* **2019**, *31*, 6174.
[49] X. Wang, X. Zhong, Z. Zha, G. He, Z. Miao, H. Lei, Q. Luo, R. Zhang, Z. Liu, L. Cheng, *Appl. Mater. Today* **2020**, *18*, 100464.
[50] X. Wang, J. Xu, D. Yang, C. Sun, Q. Sun, F. He, S. Gai, C. Zhong, C. Li, P. Yang, *Chem. Eng. J.* **2018**, *354*, 1141.
[51] S. Zhang, L. Wu, W. Shi, J. Qin, W. Feng, Y. Chen, R. Zhang, *Adv. Funct. Mater.* **2023**, *33*, 2302360.
[52] Y. Huang, S. Wu, L. Zhang, Q. Deng, J. Ren, X. Qu, *ACS Nano* **2022**, *16*, 4228.
[53] S. Qiu, X. Wu, Z. Li, X. Xu, J. Wang, Y. Du, W. Pan, R. Huang, Y. Wu, Z. Yang, Q. Zhou, B. Zhou, X. Gao, Y. Xu, W. Cui, F. Gao, D. Geng, *ACS Nano* **2022**, *16*, 17062.
[54] H. Wu, F. Chen, C. You, Y. Zhang, B. Sun, Q. Zhu, *Small* **2020**, *16*, 2001805.
[55] Y. Wang, W. Wang, D. Sang, K. Yu, H. Lin, F. Qu, *Biomater. Sci.* **2021**, *9*, 4473.
[56] L. An, X. Wang, X. Rui, J. Lin, H. Yang, Q. Tian, C. Tao, S. Yang, *Angew. Chem., Int. Ed.* **2018**, *57*, 15782.
[57] S. Sun, P. Li, S. Liang, Z. Yang, *Nanoscale* **2017**, *9*, 11357.
[58] J. Yu, T. I. Lee, M. Misra, *J. Ind. Eng. Chem.* **2018**, *66*, 468.
[59] Z. Pan, F. Cao, X. Hu, X. Ji, *J. Mater. Chem. A* **2019**, *7*, 8984.
[60] Y. Fu, Q. Li, J. Liu, Y. Jiao, S. Hu, H. Wang, S. Xu, B. Jiang, *J. Colloid Interface Sci.* **2020**, *570*, 143.
[61] X. Song, X. Li, D. Wei, R. Feng, T. Yan, Y. Wang, X. Ren, B. Du, H. Ma, Q. Wei, *Biosens. Bioelectron.* **2019**, *126*, 222.
[62] S. Jia, X. Li, B. Zhang, J. Yang, S. Zhang, S. Li, Z. Zhang, *Appl. Surf. Sci.* **2019**, *463*, 829.
[63] Y. Hou, J. Li, X. Gao, Z. Wen, C. Yuan, J. Chen, *Nanoscale* **2016**, *8*, 8228.
[64] H. S. Jung, J.-H. Lee, K. Kim, S. Koo, P. Verwilst, J. L. Sessler, C. Kang, J. S. Kim, *J. Am. Chem. Soc.* **2017**, *139*, 9972.
[65] Z. Fang, J. Zhang, Z. Shi, L. Wang, Y. Liu, J. Wang, J. Jiang, D. Yang, H. Bai, B. Peng, H. Wang, X. Huang, J. Li, L. Li, W. Huang, *Adv. Mater.* **2023**, *35*, 2301901.
[66] R. Ye, H. Fang, Y. Zheng, N. Li, Y. Wang, X. Tao, *ACS Appl. Mater. Interfaces* **2016**, *8*, 13879.
[67] W. Chong, B. Ng, X. Y. Kong, L. Tan, L. K. Putri, S. Chai, *Appl. Catal. B Environ.* **2023**, *325*, 122372.
[68] C. Yang, M. Wang, M. Chang, M. Yuan, W. Zhang, J. Tan, B. Ding, P. a. Ma, J. Lin, *J. Am. Chem. Soc.* **2023**, *145*, 7205.
[69] Y. Yang, T. Hu, Y. Bian, F. Meng, S. Yu, H. Li, Q. Zhang, L. Gu, X. Weng, C. Tan, R. Liang, *Adv. Mater.* **2023**, *35*, 2211205.
[70] Y. Zhao, Y. Bian, X. Xiao, B. Liu, B. Ding, Z. Cheng, P. a. Ma, J. Lin, *Small* **2022**, *18*, 2204047.
[71] F. Gao, L. Jiang, J. Zhang, Y. Chang, W. Gao, L. Ding, G. Ma, X. Ma, Y. Guo, *ACS Mater. Lett.* **2023**, *5*, 1.
[72] Y. Song, Y. Wang, Y. Zhu, Y. Cheng, Y. Wang, S. Wang, F. Tan, F. Lian, N. Li, *Adv. Healthcare Mater.* **2019**, *8*, 1900250.
[73] B. Liu, Y. Bian, S. Liang, M. Yuan, S. Dong, F. He, S. Gai, P. Yang, Z. Cheng, J. Lin, *ACS Nano* **2022**, *16*, 617.
[74] C. Yang, M. Chang, M. Yuan, F. Jiang, B. Ding, Y. Zhao, P. Dang, Z. Cheng, A. A. A. Kheraif, P. a. Ma, J. Lin, *Small* **2021**, *17*, 2100961.